

# A Multidimensional Tensor Low Rank Method for Magnetic Resonance Image Denoising

Lizhen Deng , Yuxin Cao , Zhongyang Wang , Xiaokang Wang , and Yu Wang 

**Abstract**—In this paper, we present the Magnetic Resonance Image (MRI) denoising method via nonlocal multidimensional low rank tensor transformation constraint (NLRT). We first design a nonlocal MRI denoising method by non-local low rank tensor recovery framework. Furthermore, a multidimensional low rank tensor constraint is used to obtain low-rank prior information combined with 3-dimensional structure feature of MRI image cubes. Our NLRT can achieve denoising by retaining more image detail information. The optimization and updating process of the model is solved via the alternating direction method of multipliers (ADMM) algorithm. Several state-of-the-art denoising methods are selected for comparative experiments. In order to reflect the performance of the denoising method, Rician noise with different levels is added to the experiment to analyze the results. The experimental results prove that our NLRT has more outstanding denoising ability and can obtain better MRI images.

**Index Terms**—Medical image, MRI denoise, ADMM, nonlocal tensor.

## I. INTRODUCTION

**M**EDICAL imaging is a key technology in modern medical research and is of great importance to medical treatment [1], [2], [3], [4]. Due to its benefits of high tissue and high resolution, multi-sequence imaging, magnetic resonance imaging (MRI) is a widely utilized medical imaging technology. Unfortunately, it has low resolution and large noise artifacts after reconstruction, which affects image quality and subsequent clinical diagnosis and treatment. Therefore, MRI denoising has become an important pre-processing step to improve the quality of medical examination and analysis tasks such as reconstruction or segmentation. However, it is quite difficult to maintain the denoising in whole three-dimensional MRI because of high computational cost and heavy information.

Manuscript received 21 January 2022; revised 20 March 2023; accepted 17 April 2023. Date of publication 4 May 2023; date of current version 8 August 2024. This work was supported by the National Natural Science Foundation of China under Grant 62072256. (Corresponding author: Yu Wang.)

Lizhen Deng and Yuxin Cao are with the National Engineering Research Center of Communication and Network Technology, Nanjing University of Posts and Telecommunications, Nanjing, Jiangsu 210003, China (e-mail: alicedenglzh@gmail.com; 1021010424@njupt.edu.cn).

Zhongyang Wang is with the School of Communications and Information Engineering, Nanjing University of Posts and Telecommunications, Nanjing, Jiangsu 210003, China (e-mail: wangzhongyang96210@163.com).

Xiaokang Wang is with the School of Computer Science and Technology, Hainan University, Haikou, Hainan 570228, China (e-mail: xkwang@hainanu.edu.cn).

Yu Wang is with the Science and Technology on Integrated Information System Laboratory, Institute of Software Chinese Academy of Sciences, Beijing 100190, China (e-mail: wangyuasc@163.com).

Digital Object Identifier 10.1109/TCBB.2023.3272893

In recent years, many methods have been proposed to solve the difficulty of denoising from MRIs [5], which can be summarized into several categories: filtering approach [6], transform domain approach [7] and statistical approach. The spatial filter [8] reduced the Gaussian noise in MRI by convolving the image in the spatial domain, smoothing the final image and reducing the high spatial frequencies in the image. The temporal filter can avoid blending artifacts by choosing a suitable relationship between sampling intervals. However, it cannot be widely used because too narrow a frequency response will degrade the signal at the edge of the image, or too wide a frequency response will introduce noise. The NL-means filter mainly realized the denoising by comparing image patches and estimating each pixel of the image as a weighted average of pixels in a search window. Due to its simplicity and high-denoising performance, the NL-means filter has been adapted in the denoising of MR images widely [9], [10]. Manjon et al. [11] modified the original NLM algorithm and combined the information of various channels to obtain the similarity measure between multi-spectral sequences, and then reduced the noise of multi-spectral MRI.

In addition to the filter-based method, the transform domain-based method is also a common denoising method. The principle is to project the noisy image into the transform domain to obtain the transform coefficients. This method used the separation transform coefficient between the image signal and the noise signal to achieve the denoising process [12]. Wavelet transform and block matching 3D filtering algorithms (BM3D) [13] were both common transform domain denoising algorithms. The main drawback of the wavelet transform method is that the denoising process eliminates some structural information. The BM3D algorithm combines the non-local self-similarity of the image with the wavelet transform method, which overcomes the defects of the wavelet transform to some extent. Thus, it is often used as the baseline of MRI denoising [14].

Statistical learning-based denoising methods have gradually become a research hotspot recently, especially the methods based on dictionary learning and image block prior knowledge learning. The principle of dictionary-based learning for denoising is to exploit the sparsity of images and train on a large image dataset to obtain a redundant dictionary. The trained dictionary is then used to represent the noisy images for the purpose of denoising. Although the dictionary learning-based denoising method achieved good results [15], this denoising method ignores the similarity of the images themselves. Moreover, dictionary learning itself is a very time-consuming process. Image blocks contain rich local structure information, which

can provide enough a prior information for image denoising. Meanwhile, denoising small blocks of images can reduce the computational effort and improve the computational efficiency. Yu et al. [16] demonstrated that the Gaussian mixture model and the maximum a posterior algorithm based on expectation maximization (MAP-EM) can provide a general and efficient solution to the inverse problem in image processing. Based on this, a segmented linear estimation algorithm based on image chunking is proposed to solve the image inverse problem.

In recent years, deep learning has rapidly penetrated into various fields of research [2], [17], [18], [19], [20], [21]. As research into MRI denoising continues, deep learning is beginning to be applied to this task. Compared to traditional MRI denoising algorithms, network training with deep learning avoids the problems of oversimplified parameter selection and sparse transformations. Converting the optimisation process of traditional iterative denoising algorithms to deep learning network training enables faster and more accurate denoising and reconstruction of MRI. Unlike existing MRI denoising methods that utilise spatial neighbourhood information around pixels or patches, Li et al. [22] proposed a progressive network learning strategy by fitting pixel-level and feature-level intensity distributions. The network consists of two residual blocks, one for fitting the pixel domain, one for fitting the feature domain, and one for fitting the feature domain. [23] proposed a new approach to MR image denoising using conditional generative adversarial networks (GANs). Specifically, CNNs are utilised as discriminators to remove as much noise as possible from noisy MRI images using a generator based on a convolutional encoder-decoder network. The whole architecture is trained by adversarial learning. But the limitation of deep learning strategy is its lack of adaptability. It relies excessively on k-space data for training images and scanning methods. Therefore, Hou et al. proposed an iterative method IDPCNN [24] for MRI reconstruction by combining the advantages of traditional and deep learning methods. Denoising and projection are the two phases that make up the approach. The denoising step uses a state-of-the-art denoiser to smooth the image. The projection stage investigates a prior information from the frequency domain and iteratively adds details to the spatial domain.

To improve the performance of 3D MR image denoising, this paper uses 3D operators to characterize MR images. Similar patches are filtered collaboratively while maintaining the natural 3D morphology of MRI. Based on the similarity of the patches with same size, multi-dimensional data sets of MR images are grouped into multiple groups. The use of high-dimensional matching blocks allows for the capture of local correlations for each 3D image patch and non-local correlations for different image patches. And since the nonlocal low rank constraint equilibrium matrix scheme is very balanced, imposing NLRT a prior on these tensors can effectively learn the correlation of the three modes. Thus, NLRT can effectively understand the correlation between spatial, spectral and non-local modes in multidimensional 3D MR images with low-rank prior information. The optimization-as-update process designs the classical ADMM algorithm into an MRI reconstruction framework. The framework is able to use existing image denoising

methods as a prior knowledge for reconstruction. It has the advantages of fewer parameters and more stable influence of parameter size on reconstruction quality. On the other hand, it is able to apply relatively mature image denoising methods to ADMM reconstruction, which makes the framework extensive.

In this paper, we study MRI denoising algorithms based on nonlocal low-rank tensor transform constraints, with the following main contributions:

- We exploit the low-rank nature of high-dimensional images and the advantages of tensor decomposition in processing high-dimensional data by combining the 3D structural features of the MRI image cube with non-local low-rank regularisation terms to obtain a prior information on the image features.
- The correlation between MRI spatial modes, interlaminar modes and non-local domain modes can be effectively captured by forming four-dimensional tensor feature expressions using raw image features and low-rank features. And the ADMM method is used to decompose it into four subproblems to be solved optimally in separate iterations.
- In order to analyse the denoising performance of NLRT, this paper conducts extensive experiments by comparing the experimental results of several advanced denoising methods on different MRI datasets and the effectiveness of low-rank denoising is verified by ablation studies.

The rest of the paper is organized as follows: Section II presents a review of low-rank constraint and tensor decomposition methods, providing a detailed description of some algorithms belonging to these classes. Section III is devoted to the model of our proposed algorithm and the optimization process of ADMM. Section IV reports extensive experimental simulations, as well as a detailed discussion of the results. Finally, Section V draws conclusions.

## II. RELATED WORK

### A. Low Rank Constraint

The mathematical representation of an image is usually described in the form of a matrix. The rows and columns of the matrix correspond to the height and width of the image, and the elements of the matrix correspond to the intensity values at the corresponding pixel positions of the image. The processing of digital images is often done by means of matrices, and the properties of matrix rank are also applicable in image processing [25], [26], [27], [28], [29], [30]. The rank of the image matrix can indicate the richness of information in an image. The elements in the image matrix are arbitrary and can represent the structure of the image, the color, and the surrounding pixel points. In addition, there are many non-locally similar regions in the images, so the rank of all natural images is very low. If there is too much noise in an image, it will add extra clutter information to the image and break the low-rankness of the image. The low rank of an image indicates that it contains a large amount of redundant information, which can be used for the denoising process of noisy images and also for the recovery of missing images. Because low-rank priors can effectively learn data redundancy and self-similarity, low-rank learning has been widely

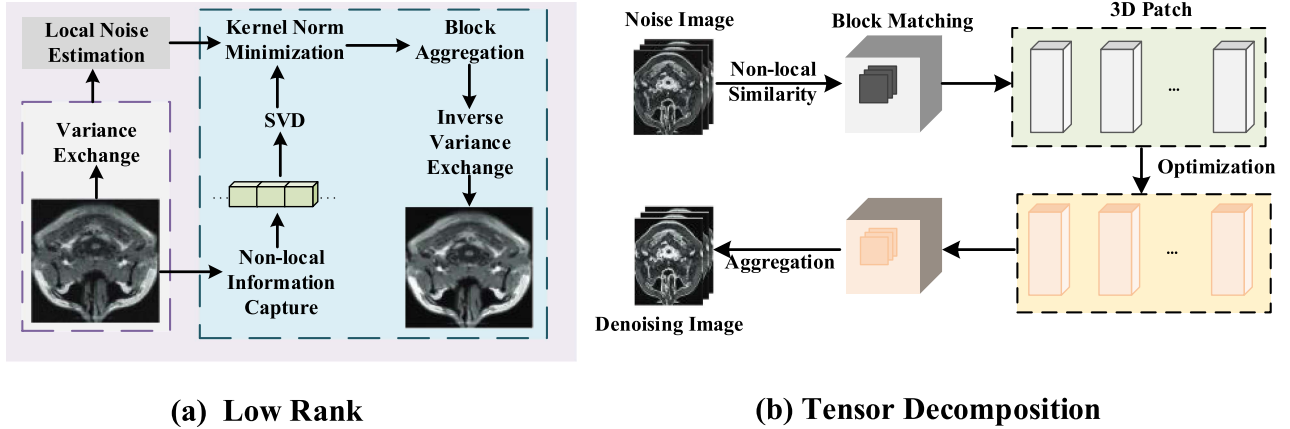


Fig. 1. (a) The weighted kernel norm low-rank constraint denoising process. (b) The three-dimensional tensor decomposition denoising process.

used for matrix completion [31], image fusion [32], clustering [33], and pattern recognition [34]. The MRI downsampling data reconstruction non-local mean method developed in recent years exploits the similarity and redundancy between blocks. Dong et al. [35] first combined the nonlocal similarity method with the low-rank method to reconstruct MRI images using the low-rank property of nonlocal bidirectional differencing. They proposed to use the spatially adaptive iterative solar value thresholding (SAIST) algorithm to solve the problem, which improved the computational efficiency and reconstruction quality compared with the BM3D algorithm. Haldar [36] proposed the low-rank model for local k-domain (LORAKS), which improves the flexibility of the MR reconstruction framework and is easily extended to parallel imaging applications. Yoon et al. [37] also introduced motion compensation based on the block low-rank method, which effectively improves the sparsity of the data. In the process of structured low-rank model research, the reconstruction algorithm of this model is also a research hotspot because the computation is usually large. In this paper, the ADMM is optimally solved by using the augmented Lagrangian function which is based on the low-rank algorithm. This can further improve the reconstruction accuracy and reduce the computational complexity.

### B. Tensor Decomposition

In practical applications, the vast majority of data is three-dimensional or even higher dimensional. Traditional data representation methods based on scalars, vectors and matrices are obviously difficult to fully represent such high-dimensional data and its internal structure. Classical methods (e.g., PCA, SVM, etc.) only vectorize or matrixize high-dimensional data before analyzing and studying them. The data spatial structure is often ignored, leading to the problem of corrupted data spatial structure. Vectorization or matrixization of high-dimensional data also result in larger dimensional vectors or matrices, which requires more storage and computation for computers. Tensor expressions [38] have received much attention because of their outstanding advantages. As one of the most popular tensor representation methods, the tensor training (TT) method defines a

new tensor level called TT level. TT level includes a matrix level formed by balanced matrix format, i.e., the tensor is constructed as a matrix along the pattern arrangement. Tensor decomposition avoids the damage caused by vectorization or matrixization of high-dimensional data. Since matrices have many similar features to each other, tensor can be seen as a generalization of matrices. Zeng et al. [39] proposed a tensor sparse method based on Kronecker basis representation and applied it to the field of CT imaging. Yu et al. [40] proposed a CS-DMRI reconstruction method based on tensor sparse decomposition, which uses tensor higher-order singular value decomposition (HOSVD) to DMR signal to perform sparse processing. Yang et al. [41] proposed to add a weighted Schatten parameter method to the expansion matrix of each mode of the tensor as the low-rank regular term of the reconstructed model, and finally solved the optimization problem using the Bregman iterative algorithm.

## III. OUR PROPOSED METHOD

### A. The Proposed NLRT Method

The Fig. 2 shows the formation process of the 4-D tensor rank constraint of the MR image and the objective function. As shown in the Fig. 2, the  $k^{th}$  group can constitute a 4-D tensor  $\mathcal{Z}^k \in \mathbb{R}^{d_L \times d_W \times d_H \times N_k}$ , which has four modes, i.e., length mode, width mode, height mode and nonlocal mode. Inspired by tensor training [42], [43], the following will introduce our tensor low rank constraint function in detail.

In general, the rank constraint of a matrix  $M$  is nonconvex and hard to optimize, thus the nuclear norm  $\|M\|_*$  is usually used to replace the rank constraint, which is defined as

$$\|M\|_* = \sum_i \sigma_i(M) \quad (1)$$

where  $\sigma_i(M)$  denotes the  $i$ -th singular value of the matrix  $M$ . Then the matrix can get the closed-form solution by singular value decomposition(SVD). According to [44], the log sum of singular values is more effective to solve the rank minimization problems, which can be defined as  $\sum_i \log(\sigma_i(M) + \epsilon)$ .

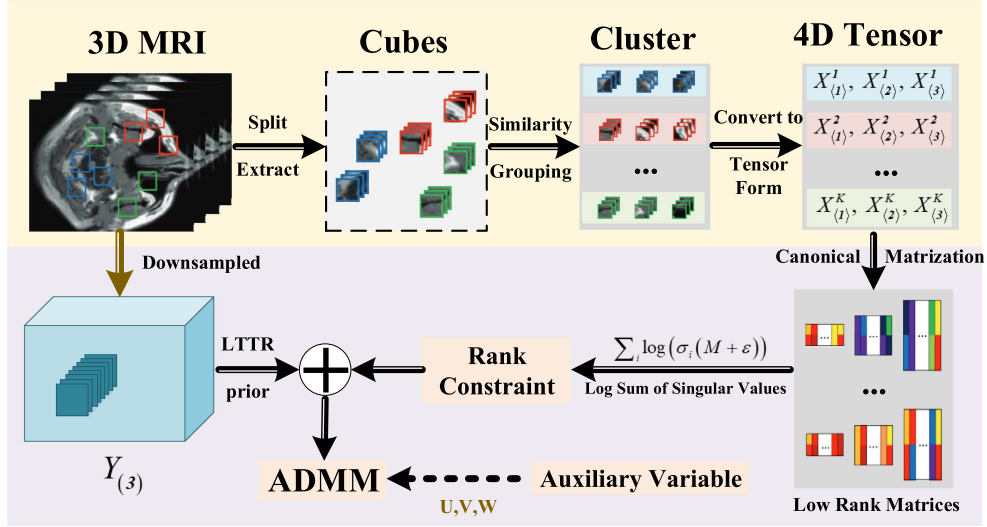


Fig. 2. Illustration of NLRT of 3-D MR images. The 3-D MRI is first decomposed and feature extracted, and the feature cubes are classified for similarity, and then constrained using low rank after conversion into a 4-D tensor. For algorithm optimization we introduce Lagrange multipliers with three each auxiliary variables for ADMM iterative solution.  $Y_{(3)}$  is the three mode examination matrix of the sampled version of the 4-D tensor  $Z$ .

Taking the log sum into the tensor to consider, the rank constraint of 4-D tensor  $Z^k$  can be defined as:

$$\|Z^k\|_{RC} = \sum_{t=1}^3 \alpha_t \sum_i \log(\sigma_i(M) + \varepsilon) \quad (2)$$

where  $\alpha_t$  is the trade-off parameter, which is defined as follows:

$$\alpha_t = \frac{\sqrt{\beta_t}}{\sum_{t=1}^3 \sqrt{\beta_t}},$$

$$\beta_t = \min \left( \prod_{j=1}^t I_j \prod_{j=t}^3 I_j \right), t = 1, 2, 3 \quad (3)$$

where  $I_j$  denotes the dimension of  $j^{th}$  mode of tensor  $Z^k$ . The rank constraint  $\|Z^k\|_{TT}$  contains the rank of matrices  $Z_{(1)}^k \in \mathbb{R}^{d_L \times d_W \times d_H \times N_k}$ ,  $Z_{(2)}^k \in \mathbb{R}^{d_L \times d_W \times d_H \times N_k}$ ,  $Z_{(3)}^k \in \mathbb{R}^{d_L \times d_W \times d_H \times N_k}$ ,  $Z_{(1)}^k$  constrains the pixel information,  $Z_{(2)}^k$  presents the image information, and  $Z_{(3)}^k$  represents the features among the tensor cubes.

Because the well-balanced matricization scheme of TT rank can effectively learn the correlation between spatial patterns, spectral patterns and nonlocal patterns, this paper combines the low tensor-train rank (LTTR) of TT rank optimization with NLRT to impose LTTR constraints on the model, and we can get the following optimization problems:

$$\min_{X_{(3)}} \|Y_{(3)} - X_{(3)}\|_F^2 + \lambda \sum_{k=1}^K \|X^k\|_{RC} \quad (4)$$

where  $\lambda$  is the rank constraint regularization parameter. Combining with (2), the above optimization problem is equivalent as

$$\min_{X_{(3)}} \|Y_{(3)} - X_{(3)}\|_F^2 + \lambda \sum_{k=1}^K \sum_{t=1}^3 \alpha_t \log(\sigma_i(X_{(t)}^k) + \varepsilon) \quad (5)$$

## B. Optimization

For the proposed model is an unconstrained optimization problem, We utilize the ADMM framework to handle the problem.

By introducing three variables  $U = X$ ,  $V = X$  and  $W = X$ . The augmented Lagrangian function is shown as follows:

$$L(U, V, W, X, O, P, Q) = \|X_{(3)} - X_{(3)}\|_F^2 + \mu \left\| U - X + \frac{O}{2\mu} \right\|_F^2$$

$$+ \lambda \sum_{k=1}^K \alpha_1 \log(\sigma_i(U_{(1)}^k) + \varepsilon) + \mu \left\| V - X + \frac{P}{2\mu} \right\|_F^2$$

$$+ \lambda \sum_{k=1}^K \alpha_2 \log(\sigma_i(V_{(2)}^k) + \varepsilon) + \mu \left\| W - X + \frac{Q}{2\mu} \right\|_F^2$$

$$+ \lambda \sum_{k=1}^K \alpha_3 \log(\sigma_i(W_{(3)}^k) + \varepsilon) \quad (6)$$

where  $O$ ,  $P$  and  $Q$  are the Lagrangian multipliers and  $\mu$  is the penalty parameter. The augmented Lagrangian function can be minimized by iteratively solving the following subproblems:

- *Denoising Module.*

$$X = \arg \min_X L(U, V, W, X, O, P, Q)$$

$$= \arg \min_X \|Y_{(3)} - X_{(3)}\|_F^2 + \mu \left\| U - X + \frac{O}{2\mu} \right\|_F^2$$

$$+ \mu \left\| V - X + \frac{P}{2\mu} \right\|_F^2 + \mu \left\| W - X + \frac{Q}{2\mu} \right\|_F^2 \quad (7)$$

The formula mentioned above is strong convex. Therefore,  $X_{(3)}$  can be solved by gradient descent:

$$X_{(3)} = [(3\mu + 1)I]^{-1} \left[ Y_{(3)} + \mu \left( U_{(3)} + \frac{O_{(3)}}{2\mu} \right) \right]$$

$$+ \mu \left( V_{(3)} + \frac{P_{(3)}}{2\mu} \right) + \mu \left( W_{(3)} + \frac{Q_{(3)}}{2\mu} \right) \Big] \quad (8)$$

where  $U_{(3)}, V_{(3)}, W_{(3)}, O_{(3)}, P_{(3)}$  and  $Q_{(3)}$  are three-mode unfolding matrices of tensors  $\mathcal{U}, \mathcal{V}, \mathcal{W}, \mathcal{O}, \mathcal{P}$  and  $\mathcal{Q}$ , respectively.  $I \in \mathbb{R}^{d_H \times d_H}$  is the identity matrix.

- *Pixel-level Feature.*

$$U = \arg \min_U L(U, V, W, X, O, P, Q)$$

$$= \arg \min_U \mu \left\| U - X + \frac{O}{2\mu} \right\|_F^2 + \lambda \sum_{k=1}^K \alpha_1(U_{(1)}^k) \quad (9)$$

The above problem can be separately solved for each cluster, i.e.,

$$\arg \min U \mu \left\| U - X + \frac{O}{2\mu} \right\|_F^2 + \lambda \sum_{k=1}^K \alpha_1(U_{(1)}^k) \quad (10)$$

where  $U_{(1)}^k, X_{(1)}^k$  and  $Q_{(1)}^k$  are the mode-1 canonical matrices of tensors  $U^k, X^k, O^k$ . The 4-D tensors  $U^k, X^k, O^k$  are constituted by  $k^{th}$  cube cluster in  $U^k, X^k, O^k$ , respectively. The optimization problem has the following solution:

$$U_{(1)}^k = U_1^k \widetilde{\sum}_1^k V_1^k, 1 \leq k \leq K \quad (11)$$

where and are acquired by the SVD, i.e.,  $X_{(1)}^k - \left( \frac{O_{(1)}^k}{2\mu} \right) = U_1^k \widetilde{\sum}_1^k V_1^k$ .  $\widetilde{\sum}_1^k$  is the diagonal matrix. After obtain mode-1 canonical matrix  $U_{(1)}^k$ , we can acquire tensor  $U^k$  via  $U^k = fold_1(U_{(1)}^k)$ , and  $U$  is obtained by placing the cube clusters  $U^k, 1 < k < K$ , into the corresponding positions.

- *Image-level Feature.*

$$V = \arg \min_V L(U, V, W, X, O, P, Q)$$

$$= \arg \min_V \mu \left\| V - X + \frac{P}{2\mu} \right\|_F^2 + \lambda \sum_{k=1}^K \alpha_2(V_{(2)}^k) \quad (12)$$

- *Cube-level Feature.*

$$W = \arg \min_W L(U, V, W, X, O, P, Q)$$

$$= \arg \min_W \mu \left\| W - X + \frac{Q}{2\mu} \right\|_F^2 + \lambda \sum_{k=1}^K \alpha_3(W_{(3)}^k) \quad (13)$$

The solution process of  $V$  and  $W$  is consistent with the solution of  $U$ , which is not fully shown here.

#### IV. DENOISING EXPERIMENTS

In this section, in order to evaluate the proposed method, we take use of the well-known BrainWeb 3D MRI datasets [45] which contains the noise-free T1 weighted dataset (T1w), T2

weighted dataset (T2w) and proton weighted dataset (PDw). The size of the MR image data is  $181 \times 217 \times 181$  with  $1 \times 1 \times 1 \text{ mm}^3$ . Similar to [46], we add varying levels of Rician noise (1 – 9% of maximum intensity). Rician noise [47] which is not additive was generated by adding Gaussian noise to real and imaginary parts and then computing the magnitude images. In addition, we analyze the performance of all denoising models by comparing the values of quantitative measures and visual graphs. All experiments are implemented in MATLAB on two RTX3090TI GPUs.

#### A. Metrics and Comparison Methods

To evaluate the performance of denoising methods, we mainly use three quantitative measures.

- The first one is the mean square error (MSE) between the denoised data and ground truth, defined as follows:

$$MSE = \frac{1}{H \times W} \sum_{i=1}^H \sum_{j=1}^W [X(i, j) - Y(i, j)]^2 \quad (14)$$

where  $(i, j)$  represents the pixel location,  $X$  is the given target image,  $Y$  is the reconstructed image, and  $H$  and  $W$  represent the height and width of the image, respectively.

- The second quantitative measure is the structural similarity index (SSIM), which is consistent with human eye perception. SSIM is a full-reference image quality evaluation index, which measures image similarity in terms of brightness, contrast, and structure. The value range of SSIM is  $[0, 1]$ . The larger the value, the smaller the image distortion. It is defined as follows:

$$SSIM = \frac{(2\mu_y \mu_{\tilde{y}} + c_1)(2\sigma_{y\tilde{y}} + c_2)}{(\mu_y^2 + \mu_{\tilde{y}}^2 + c_1)(\sigma_y^2 + \sigma_{\tilde{y}}^2 + c_2)} \quad (15)$$

where  $\mu_y$  and  $\mu_{\tilde{y}}$  are mean value of images  $y$  and  $\tilde{y}$ ,  $\sigma_y$  and  $\sigma_{\tilde{y}}$  are the standard deviation of images  $y$  and  $\tilde{y}$ ,  $\sigma_{y\tilde{y}}$  is the covariance of  $y$  and  $\tilde{y}$ ,  $c_1$  and  $c_2$  are constants.

- The last quantitative measure is the peak signal-to-noise ratio (PSNR), which is the most common and widely used objective measurement method to evaluate image quality. PSNR calculates the similarity between two images and evaluates the noise intensity of a denoised image relative to the original image. However, it is based on the error between corresponding pixels, that is, based on error-sensitive image quality evaluation. A larger value of PSNR indicates better quality. The MSE-based definition of PSNR is as follows:

$$PSNR = 10 * \log_{10} \frac{MAX^2}{MSE} \quad (16)$$

In order to evaluate the noise suppression ability of the proposed method, we selected four representative methods for comparison experiments, and several methods are briefly described below.

- *ANLM [10]*. ANLM, the so-called adaptive non-local mean filter, mainly deals with MRI with spatially varying noise levels. It uses a new local noise estimation method to automatically obtain information about the local image

TABLE I  
PSNR, SSIM AND MSE PERFORMANCE COMPARISON OF NOISY OBSERVATION FOR ANLM, MNLM3D, SANLM3D, PRINLM3D AND OUR NLRT ON T1w DATABASES. THE BEST VALUES ARE MARKED IN RED

Dataset	Filter	Metrics	$\sigma(\%)$								
			1	2	3	4	5	6	7	8	9
T1w	NLRT	PSNR	<b>44.35</b>	<b>40.56</b>	<b>38.43</b>	<b>36.85</b>	<b>35.73</b>	<b>34.72</b>	<b>34.19</b>	<b>33.41</b>	<b>31.98</b>
		SSIM	<b>0.9973</b>	<b>0.9843</b>	<b>0.9813</b>	<b>0.9659</b>	<b>0.9628</b>	<b>0.9584</b>	<b>0.9473</b>	0.9256	<b>0.9128</b>
		MSE	1.79	<b>3.31</b>	<b>5.54</b>	<b>7.73</b>	<b>10.14</b>	<b>12.78</b>	<b>16.39</b>	<b>18.83</b>	<b>21.64</b>
	ANLM	PSNR	43.41	39.96	37.86	36.29	35.04	33.99	33.07	32.25	31.5
		SSIM	0.991	0.9821	0.9722	0.9612	0.9492	0.9361	0.9219	0.907	0.8916
		MSE	1.69	3.75	6.08	8.71	11.62	14.81	18.29	22.09	26.26
	PRINLM3D	PSNR	43.97	40.41	38.19	36.59	35.34	34.29	33.37	32.61	31.94
		SSIM	0.9906	0.9821	0.974	0.9634	0.9502	0.9425	0.9383	<b>0.9263</b>	0.9122
		MSE	<b>1.48</b>	3.37	5.62	8.13	10.85	13.81	17.08	20.39	23.75
	SANLM3D	PSNR	43.16	39.74	37.66	36.11	34.86	33.81	32.89	32.07	31.31
		SSIM	0.9932	0.9818	0.9767	0.9629	0.9552	0.9395	0.924	0.9038	0.8994
		MSE	1.79	3.94	6.36	9.09	12.12	15.45	19.09	23.07	27.43
	MNLM3D	PSNR	42.83	40.33	37.33	35.48	35.28	34.17	30.18	28.54	25.88
		SSIM	0.9876	0.9795	0.9725	0.9651	0.9517	0.9427	0.9317	0.9061	0.886
		MSE	1.96	3.98	5.89	9.22	13.68	14.54	22.94	20.37	34.68

noise level from the image to adjust the denoising strength of the filter.

- *PRINLM3D* [48]. The pre-filtered rotationally invariant non-local mean filter (PRINLM3D) is based on a 3D moving window discrete cosine transform hard threshold segmentation and a 3D rotationally invariant non-local mean filter. It has a run time of less than 1 minute and is available in most clinical and research settings.
- *SANLM3D* [10]. Spatial adaptive nonlocal mean (SANLM) uses Gaussian kernel spatial smoothing as a preprocessing step to average time series from spatially adjacent voxels. It blurs the tissue boundaries and reduces the spatial resolution, thus smoothing the common multi-band EPI (mEPI) noise and improving the tissue specificity of the default network mapping.
- *MNLM3D* [49]. Adaptive multi-resolution block-domain non-local mean filtering (MNLM) based on adaptive soft wavelet coefficient mixing implicitly adjusts the amount of denoising based on the spatial and frequency information contained in the image, which can effectively remove noise while maintaining fine structure.

## B. Evaluation on Synthetic Data

1) *Quantitative Analysis*: The detailed denoising results of our NLRT, ANLM, PRI-NLM3D, SANLM3D, and MNLM3D are reported in Tables I, II, and III. Each denoising model was tested on three data sets (T1w, T2w, PDw), and the performance of the experiment was demonstrated by three indicators (PSNR, SSIM, MSE). The values in each row of the table are

obtained under different conditions of Rician noise. In order to highlight the comparison results, we mark the optimal value of the indicator under each condition in red. As can be seen from Tables I, II, and III, NLRT has an excellent performance in the experiment.

In the table, when  $\sigma = 1\%$  and  $\sigma = 8\%$ , the best performance of MSE and SSIM is PRINLM3D. Because PRINLM3D makes use of sparsity and self-similarity to pay more attention to the elimination of artifacts and other problems in the process of denoising. The model in this paper is aimed at high-dimensional tensor structure, and combined with low-rank can better capture the correlation between different modes, and maintain the detailed texture and overall contour of the image. Except for a few cases, NLRT obtains the best indicators, especially on the PDw dataset. Even if the best results are not obtained, the performance metric value obtained by our method is not much different from the first one. For example, under the condition that  $\sigma = 8\%$ , the SSIM values of our method are only 0.076% and 0.032% less than the first place on T1w and T2w datasets, respectively. And if the  $\sigma$  value is 1%, MSE value of NLRT method ranks second, which is 0.31 larger than PRINLM3D. When  $\sigma > 1$ , the MSE value of our NLRT is optimal. On the whole, the performance of all denoising models decreases with the increase of the noise ratio, the performance of our model under less noise is much better than that with more noise, and it is much competitive than other methods.

2) *Qualitative Analysis*: To clearly illustrate the performance of the comparison method, we choose to compare the results of the three datasets together to better compare the advantages and disadvantages. Fig. 3 provide visual evaluations of

TABLE II  
PSNR, SSIM AND MSE PERFORMANCE COMPARISON OF NOISY OBSERVATION FOR ANLM, MNLM3D, SANLM3D, PRINLM3D AND OUR NLRT ON T2w DATABASES. THE BEST VALUES ARE MARKED IN RED

Dataset	Filter	Metrics	$\sigma(\%)$								
			1	2	3	4	5	6	7	8	9
T2w	NLRT	PSNR	<b>42.91</b>	<b>38.41</b>	<b>35.94</b>	<b>34.27</b>	<b>32.75</b>	32.43	<b>30.74</b>	<b>29.97</b>	28.94
		SSIM	<b>0.9968</b>	<b>0.9938</b>	<b>0.9864</b>	<b>0.9738</b>	<b>0.9626</b>	<b>0.9585</b>	0.9447	0.9379	<b>0.9284</b>
		MSE	<b>2.35</b>	<b>5.31</b>	<b>9.32</b>	<b>15.81</b>	<b>19.79</b>	<b>26.79</b>	<b>33.89</b>	<b>39.66</b>	<b>47.11</b>
	ANLM	PSNR	38.85	36.20	34.36	32.98	31.90	30.99	30.21	29.50	28.86
		SSIM	0.9893	0.9799	0.9702	0.9601	0.9495	0.9389	0.9281	0.9170	0.9056
		MSE	5.14	9.46	14.46	19.86	25.50	31.41	37.64	44.27	51.29
	PRINLM3D	PSNR	42.06	37.69	35.28	33.69	32.41	31.39	30.44	29.66	<b>28.95</b>
		SSIM	0.9952	0.9889	0.9785	0.9693	0.9583	0.9578	<b>0.9456</b>	0.9382	0.9273
		MSE	2.45	6.71	11.69	16.84	22.64	28.61	35.59	42.61	50.16
	SANLM3D	PSNR	38.28	35.81	34.05	32.72	31.65	30.75	29.97	29.27	28.63
		SSIM	0.9927	0.9852	0.9782	0.9638	0.9563	0.9438	0.9374	0.9197	0.9063
		MSE	5.87	10.36	15.52	21.10	26.99	33.20	39.75	46.71	54.08
	MNLM3D	PSNR	40.06	37.69	35.02	32.24	30.15	<b>32.84</b>	28.46	28.64	26.73
		SSIM	0.9895	0.9875	0.9753	0.9659	0.9504	0.9469	0.9448	0.9337	0.9094
		MSE	4.87	7.40	13.64	22.37	24.38	29.79	41.04	44.79	56.16

TABLE III  
PSNR, SSIM AND MSE PERFORMANCE COMPARISON OF NOISY OBSERVATION FOR ANLM, MNLM3D, SANLM3D, PRINLM3D AND OUR NLRT ON PDw DATABASES. THE BEST VALUES ARE MARKED IN RED

Dataset	Filter	Metrics	$\sigma(\%)$								
			1	2	3	4	5	6	7	8	9
PDw	NLRT	PSNR	<b>44.13</b>	<b>40.03</b>	<b>37.73</b>	<b>36.12</b>	<b>34.88</b>	<b>33.95</b>	<b>33.13</b>	<b>32.42</b>	<b>31.50</b>
		SSIM	<b>0.9923</b>	<b>0.9827</b>	<b>0.9728</b>	<b>0.9625</b>	<b>0.9519</b>	<b>0.9453</b>	<b>0.9359</b>	<b>0.9264</b>	<b>0.9153</b>
		MSE	<b>1.54</b>	<b>3.95</b>	<b>6.70</b>	<b>9.71</b>	<b>12.93</b>	<b>16.02</b>	<b>19.32</b>	<b>22.76</b>	<b>28.17</b>
	ANLM	PSNR	41.31	38.34	36.32	34.80	33.62	32.66	31.84	31.12	30.48
		SSIM	0.9891	0.9781	0.9655	0.9517	0.9374	0.9231	0.9087	0.8943	0.8799
		MSE	2.94	5.83	9.29	13.15	17.27	21.55	26.03	30.71	35.62
	PRINLM3D	PSNR	43.46	39.15	37.01	35.40	34.09	33.01	32.03	31.22	30.53
		SSIM	0.9906	0.9816	0.9704	0.9614	0.9514	0.9427	0.9258	0.9175	0.9049
		MSE	1.79	4.83	7.92	11.48	15.49	19.89	24.90	30.05	35.19
	SANLM3D	PSNR	40.83	38.01	36.07	34.60	33.45	32.49	31.66	30.94	30.28
		SSIM	0.9917	0.9814	0.9685	0.9587	0.9487	0.9287	0.9109	0.8967	0.8737
		MSE	3.28	6.28	9.82	13.77	17.98	22.42	27.10	32.02	37.23
	MNLM3D	PSNR	42.46	37.69	35.92	33.24	32.21	32.64	30.42	28.79	28.13
		SSIM	0.9884	0.9808	0.9724	0.9549	0.9487	0.9385	0.9173	0.8836	0.8767
		MSE	3.47	6.78	10.53	14.34	18.83	25.79	33.42	39.59	47.13

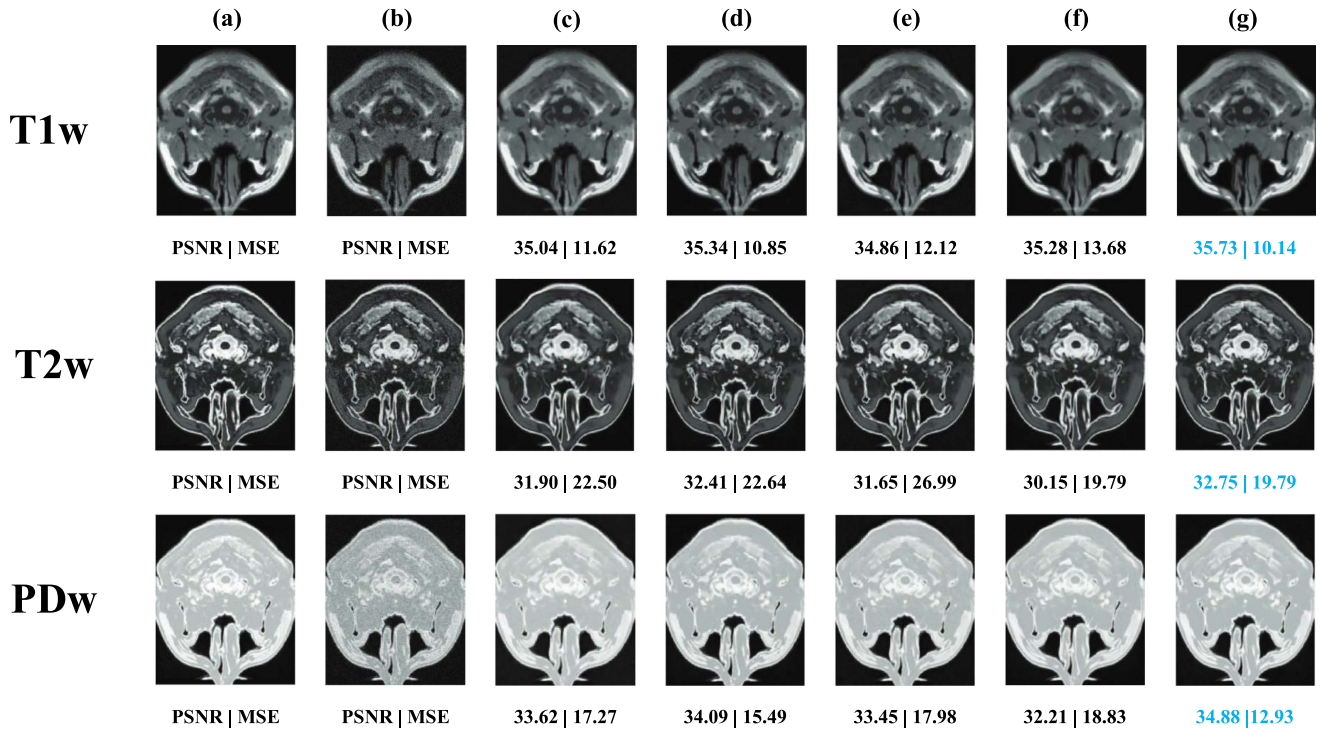


Fig. 3. Example denoising results of compared methods on T1w, T2w and Pdw corrupted with 5% Rician noise. From left to right: clean image, noisy image, ANLM, PRINLM3D, SANLM3D, MNLM3D and our NLRT. The corresponding PSNR and MSE values of the result plots are shown below each graph, where the best results are marked in blue, i.e. the metrics of NLRT.

denoising results of T1w, T2w and PDw datasets corrupted with 5% Rician-distributed noise, respectively. It should be noted that the PSNR and MSE values are marked under each sub-picture. These two values are obtained after denoising the single picture, which is different from the average value of the indicators in the table mentioned above.

As can be seen from these images, the NLRT method is more effective than the other methods in terms of both the overall profile and the degree of denoising. In Fig. 2, although the PSNR values of both ANLM and MNLM3D are above 35 on the T1w dataset, the overall image after denoising by these two methods is still blurrier and loses a lot of detailed textures, which means that the image is heavily smoothed and the quality of the image after denoising is not excellent enough. Although SANLM3D retains the detailed texture information better, the PSNR value is lower and the image denoising is not thorough enough. The difference of image details between the denoised visual image of PRINLM3D and the denoised image of NLRT method cannot be seen directly, but the PSNR and MSE values under each image prove that the denoising performance of our method is better than that of PRINLM3D, and the PSNR of NLRT is higher than that of PRINLM3D by 1.11%. T2w dataset and PDw dataset with similar results. Although the performance of the MNLM3D method is reduced, our NLRT still maintains optimality, with PSNR values of 1.05% and 2.32% higher than the second best PRINLM3D for both plots, respectively. Therefore, on the whole, the quality of NLRT after denoising is more competitive than the other compared methods.

### C. Discussion

1) *Parameter Analysis*: As discussed above, the 3D image patches with same size are grouped into multiple groups according to their similarity. However, the actual value of the number of the groups  $K$  is not sure at first. Therefore, it is necessary and important to find the best value of  $K$ . In addition, the value of  $\lambda$  also has an important influence on the grouping process. Table IV show that the experiments based on different values of  $K$  or  $\lambda$  which are under fixed conditions obtain different PSNR values. The experiment was carried out on the brainweb data and the real data. The experimental settings were the same as before, with 5% Rician noise added. As shown in Table IV,  $\lambda$  takes 0.01 and the group number  $K$  is taken from 6 to 96 at intervals of 10. Our model has the highest PSNR experimentally obtained on the brain map and the real database if  $K$  is 16. As the value of  $K$  increases, the value of PSNR decreases gradually. The main reason is that if the value of  $K$  is small, the information of the formed four-dimensional matrix is not enough, and if the value of  $K$  is too large, the number of clusters becomes dense and the similarity of 3D image blocks between different clusters also becomes higher, so that the data features are redundant which will become serious with the bigger  $K$  and affect the experimental effect. In Table IV, we fixed the  $K$  value to the optimal value 16. Similarly, both databases obtained the highest PSNR when  $\lambda = 0.01$ , that is, the best denoising performance. And Fig. 4 shows the PSNR curves with the changing values of  $K$  and  $\lambda$ .

TABLE IV  
PSNR VALUES BASED ON DIFFERENT  $K$  AND  $\lambda$  ON BRAINWEB DATA AND REAL DATA

5%Rician	Metric	K									
		6	16	26	36	46	56	66	76	86	96
Brainweb data	PSNR	32.49	<b>34.45</b>	33.83	33.17	32.74	31.98	31.22	31.09	31.42	31.01
Real data	PSNR	38.57	<b>41.39</b>	41.22	41.16	41.14	41.08	41.02	39.89	39.82	39.81
5%Rician	Metric	$\lambda * 10^{-3}$									
		0.2	0.4	0.6	2	4	6	8	10	12	14
Brainweb data	PSNR	30.83	31.94	33.42	33.64	33.89	34.02	34.27	<b>34.45</b>	34.38	34.11
Real data	PSNR	36.57	37.39	39.24	39.93	40.58	40.81	41.14	<b>41.39</b>	41.17	40.99

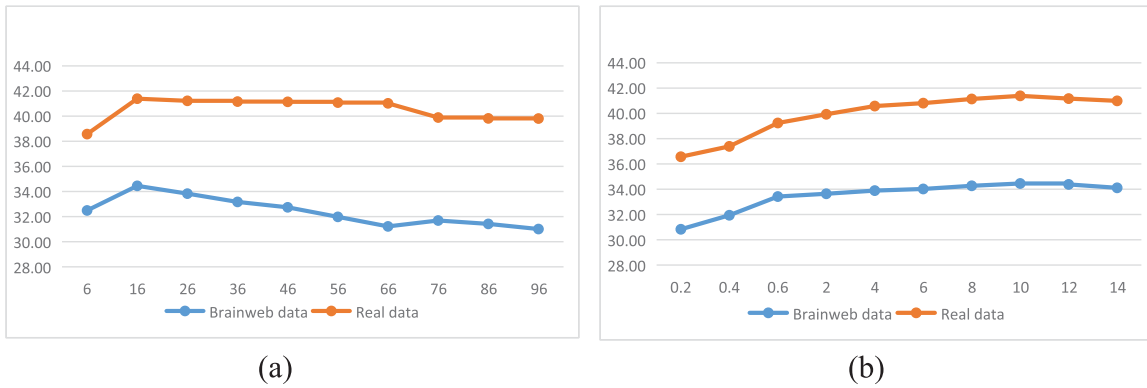


Fig. 4. PSNR curves as a function of parameters K and  $\lambda$  for our NLRT method. (a) Number of groups K. (b) Regularization parameter  $\lambda$ .

TABLE V

REGARDING THE NLRT WITH NO LOW-RANK CONSTRAINTS ON THE PDW DATASET FOR THE ABLATION EXPERIMENTS, THE BEST RESULTS ARE MARKED IN RED

Dataset	Filter	Metrics	$\sigma(\%)$								
			1	2	3	4	5	6	7	8	9
PDw	w/o NLRT	PSNR	41.09	36.87	34.47	33.02	31.29	30.41	29.94	28.89	28.05
		SSIM	0.9516	0.9409	0.9306	0.9198	0.9086	0.9007	0.8913	0.8821	0.8692
		MSE	3.97	7.12	11.05	14.24	17.57	21.36	25.98	27.43	35.86
	NLRT	PSNR	<b>44.13</b>	<b>40.03</b>	<b>37.73</b>	<b>36.12</b>	<b>34.88</b>	<b>33.95</b>	<b>33.13</b>	<b>32.42</b>	<b>31.50</b>
		SSIM	<b>0.9923</b>	<b>0.9827</b>	<b>0.9728</b>	<b>0.9625</b>	<b>0.9519</b>	<b>0.9453</b>	<b>0.9359</b>	<b>0.9264</b>	<b>0.9153</b>
		MSE	<b>1.54</b>	<b>3.95</b>	<b>6.70</b>	<b>9.71</b>	<b>12.93</b>	<b>16.02</b>	<b>19.32</b>	<b>22.76</b>	<b>28.17</b>

2) *Ablation Experiment*: The non-local low-rank tensor transformation constraint has the advantage of strong learning ability. In order to determine the effectiveness of the denoising strategy, we conducted ablation experiments on the image pairs in the TDw data set, and compared the results. This part of verification includes no LTTR constraint model and our proposed NLRT model. From the qualitative results in Table V, it can be seen that NLRT performs best in three indicators (i.e. PSNR, SSIM and MSE), and is the best when  $\sigma(\%) = 1$ . Therefore, it is necessary to carry out appropriate low-rank constraints on the 4-dimensional tensor to achieve the purpose

of denoising while preserving the image contour and feature information.

## V. CONCLUSION

The NLRT algorithm proposed in this paper combines the low-rank constraint information obtained from tensor training with MRI 3D image data to form a 4-dimensional tensor feature expression, and uses the ADMM method to optimize the solution. Due to the good performance of the low-rank constraint, NLRT can preserve the complete image contours with more

detailed textures while denoising. To verify the effectiveness of NLRT, three classical datasets are used in the experimental part to compare with four methods, and collectively, our method is highly competitive in terms of image quality after denoising. However, the manual modification in the parameter adjustment of Rician noise limits the flexibility of the method, which can be adjusted in an adaptive way to make further improvements in efficiency in the future.

## REFERENCES

- [1] J. Wang, L. Zhang, A. Zeng, D. Xia, J. Yu, and G. Yu, "DeepIII: Predicting isoform-isoform interactions by deep neural networks and data fusion," *IEEE/ACM Trans. Comput. Biol. Bioinf.*, vol. 19, no. 4, pp. 2177–2187, Jul./Aug. 2022.
- [2] X. Zhou, W. Liang, K. I. -K Wang, H. Wang, L. T. Yang, and Q. Jin, "Deep-learning-enhanced human activity recognition for internet of healthcare things," *IEEE Internet Things J.*, vol. 7, no. 7, pp. 6429–6438, Jul. 2020.
- [3] G. Xu, X. Deng, X. Zhou, M. Pedersen, L. Cimmino, and H. Wang, "FC-Fusion: Fractal component-wise modeling with group sparsity for medical image fusion," *IEEE Trans. Ind. Informat.*, vol. 18, no. 12, pp. 9141–9150, Dec. 2022.
- [4] X. Zhou, Y. Li, and W. Liang, "CNN-RNN based intelligent recommendation for online medical pre-diagnosis support," *IEEE/ACM Trans. Comput. Biol. Bioinf.*, vol. 18, no. 3, pp. 912–921, May/June 2021.
- [5] J. Mohan, V. Krishnaveni, and Y. Guo, "A survey on the magnetic resonance image denoising methods," *Biomed. Signal Process. Control*, vol. 9, no. 1, pp. 56–69, 2014.
- [6] A. Castiglione, A. De Santis, R. Pizzolante, A. Castiglione, V. Loia, and F. Palmieri, "On the protection of fMRI images in multi-domain environments," in *Proc. IEEE 29th Int. Conf. Adv. Inf. Netw. Appl.*, 2015, pp. 476–481.
- [7] A. Sharma and V. Chaurasia, "MRI denoising using advanced NLM filtering with non-subsampled shearlet transform," *Signal Image Video Process.*, vol. 15, no. 6, pp. 1331–1339, 2021.
- [8] E. R. McVergh, R. M. Henkelman, and M. J. Bronskill, "Noise and filtration in magnetic resonance imaging," *Med. Phys.*, vol. 12, no. 5, pp. 586–591, 1985.
- [9] Y. Gal, A. J. Mehnert, A. P. Bradley, K. McMahon, D. Kennedy, and S. Crozier, "Denoising of dynamic contrast-enhanced MR images using dynamic nonlocal means," *IEEE Trans. Med. Imag.*, vol. 29, no. 2, pp. 302–310, Feb. 2010.
- [10] J. V. Manjon, P. Coupe, L. M. Bonmati, D. L. Collins, and M. Robles, "Adaptive non-local means denoising of MR images with spatially varying noise levels," *J. Magn. Reson. Imag.*, vol. 31, no. 1, pp. 192–203, 2010.
- [11] J. Manjon, M. Robles, and N. A. Thacker, "Multispectral MRI denoising using non-local means," *Med. Image Understanding Anal.*, vol. 9, no. 4/5, pp. 41–46, 2007.
- [12] K. Sarkar, F. Bernard, K. Varanasi, C. Theobalt, and D. Stricker, "Structured low-rank matrix factorization for point-cloud denoising," in *Proc. IEEE Int. Conf. 3D Vis.*, 2018, pp. 444–453.
- [13] K. Dabov, A. Foi, V. Katkovnik, and K. Egiazarian, "Image denoising by sparse 3-D transform-domain collaborative filtering," *IEEE Transaction Image Process.*, vol. 16, no. 8, pp. 249–429, Aug. 2007.
- [14] E. M. Eksioğlu, "Decoupled algorithm for MRI reconstruction using nonlocal block matching model: BM3D-MRI," *J. Math. Imag. Vis.*, vol. 56, no. 3, pp. 430–440, 2016.
- [15] J. Chen, S. Liu, M. Huang, and J. Gao, "Dictionary learning for MRI denoising based on modified K-SVD," *J. Imag. Sci. Technol.*, vol. 61, no. 3, pp. 30 505–1, 2017.
- [16] G. Yu, G. Sapiro, and S. Mallat, "Solving inverse problems with piecewise linear estimators: From Gaussian mixture models to structured sparsity," *IEEE Trans. Image Process.*, vol. 21, no. 5, pp. 2481–2499, May 2012.
- [17] X. Zhou, X. Xu, W. Liang, Z. Zeng, and Z. Yan, "Deep-learning-enhanced multitarget detection for end-edge-cloud surveillance in smart IoT," *IEEE Internet Things J.*, vol. 8, no. 16, pp. 12 588–12 596, Aug. 2021.
- [18] X. Zhou, W. Liang, I. Kevin, K. Wang, and S. Shimizu, "Multi-modality behavioral influence analysis for personalized recommendations in health social media environment," *IEEE Trans. Computat. Social Syst.*, vol. 6, no. 5, pp. 888–897, Oct. 2019.
- [19] X. Zhou et al., "Intelligent small object detection for digital twin in smart manufacturing with industrial cyber-physical systems," *IEEE Trans. Ind. Informat.*, vol. 18, no. 2, pp. 1377–1386, Feb. 2022.
- [20] Y. Li, Y. Zhang, X. Huang, H. Zhu, and J. Ma, "Large-scale remote sensing image retrieval by deep hashing neural networks," *IEEE Trans. Geosci. Remote Sens.*, vol. 56, no. 2, pp. 950–965, Feb. 2018.
- [21] Y. Li, Y. Zhou, Y. Zhang, L. Zhong, J. Wang, and J. Chen, "DKDFN: Domain knowledge-guided deep collaborative fusion network for multi-temporal remote sensing land cover classification," *ISPRS J. Photogrammetry Remote Sens.*, vol. 186, pp. 170–189, 2022.
- [22] S. Li, J. Zhou, D. Liang, and Q. Liu, "MRI denoising using progressively distribution-based neural network," *Magn. Reson. Imag.*, vol. 71, pp. 55–68, 2020.
- [23] M. Tian and K. Song, "Boosting magnetic resonance image denoising with generative adversarial networks," *IEEE Access*, vol. 9, pp. 62 266–62 275, 2021.
- [24] R. Hou and F. Li, "IDPCNN: Iterative denoising and projecting CNN for MRI reconstruction," *J. Comput. Appl. Math.*, vol. 406, 2022, Art. no. 113973.
- [25] H. Zhang, J. Cai, W. He, H. Shen, and L. Zhang, "Double low-rank matrix decomposition for hyperspectral image denoising and destriping," *IEEE Trans. Geosci. Remote Sens.*, vol. 60, pp. 1–19, 2021.
- [26] Z. Chen, Z. Zhou, and S. Adnan, "Joint low-rank prior and difference of Gaussian filter for magnetic resonance image denoising," *Med. Biol. Eng. Comput.*, vol. 59, no. 3, pp. 607–620, 2021.
- [27] C. He, L. Sun, W. Huang, J. Zhang, Y. Zheng, and B. Jeon, "TSLRLN: Tensor subspace low-rank learning with non-local prior for hyperspectral image mixed denoising," *Signal Process.*, vol. 184, 2021, Art. no. 108060.
- [28] T. Qiu, Z. Wang, H. Liu, D. Guo, and X. Qu, "Review and prospect: NMR spectroscopy denoising and reconstruction with low-rank hankel matrices and tensors," *Magn. Reson. Chem.*, vol. 59, no. 3, pp. 324–345, 2021.
- [29] H. Zhu, H. Ni, S. Liu, G. Xu, and L. Deng, "TNLRS: Target-aware non-local low-rank modeling with saliency filtering regularization for infrared small target detection," *IEEE Trans. Image Process.*, vol. 29, pp. 9546–9558, 2020.
- [30] G. Xu, H. Wang, M. Zhao, M. Pedersen, and H. Zhu, "Learning the distribution-based temporal knowledge with low rank response reasoning for UAV visual tracking," *IEEE Trans. Intell. Transp. Syst.*, early access, Aug. 31, 2022, doi: [10.1109/TITS.2022.3200829](https://doi.org/10.1109/TITS.2022.3200829).
- [31] Q. Shi, H. Lu, and Y. M. Cheung, "Rank-one matrix completion with automatic rank estimation via L1-norm regularization," *IEEE Trans. Neural Netw. Learn. Syst.*, vol. 29, no. 10, pp. 4744–4757, Oct. 2018.
- [32] S. Yang, K. Zhang, and M. Wang, "Learning low-rank decomposition for pan-sharpening with spatial-spectral offsets," *IEEE Trans. Neural Netw. Learn. Syst.*, vol. 29, no. 8, pp. 3647–3657, Aug. 2018.
- [33] Y. Wang, L. Wu, X. Lin, and J. Gao, "Multiview spectral clustering via structured low-rank matrix factorization," *IEEE Trans. Neural Netw. Learn. Syst.*, vol. 29, no. 10, pp. 4833–4843, Oct. 2018.
- [34] P. Zhou, Z. Lin, and C. Zhang, "Integrated low-rank-based discriminative feature learning for recognition," *IEEE Trans. Neural Netw. Learn. Syst.*, vol. 27, no. 5, pp. 1018–1093, May 2016.
- [35] W. Dong, G. Shi, and X. Li, "Nonlocal image restoration with bilateral variance estimation: A low-rank approach," *IEEE Trans. Image Process.*, vol. 22, no. 2, pp. 700–711, Feb. 2013.
- [36] J. P. Haldar, "Low-rank modeling of local -space neighborhoods (LO-RAKS) for constrained MRI," *IEEE Trans. Med. Imag.*, vol. 33, no. 3, pp. 668–681, Mar. 2014.
- [37] H. Yoon, K. S. Kim, D. Kim, Y. Bresler, and J. C. Ye, "Motion adaptive patch-based low-rank approach for compressed sensing cardiac cine MRI," *IEEE Trans. Med. Imag.*, vol. 33, no. 11, pp. 2069–2085, Nov. 2014.
- [38] Z. Wang, G. Xu, X. Zhou, J. Y. Kim, H. Zhu, and L. Deng, "Deep tensor evidence fusion network for sentiment classification," *IEEE Trans. Comput. Social Syst.*, early access, Aug. 19, 2022, doi: [10.1109/TCSS.2022.3197994](https://doi.org/10.1109/TCSS.2022.3197994).
- [39] D. Zeng et al., "Low-dose dynamic cerebral perfusion computed tomography reconstruction via kronecker-basis-representation tensor sparsity regularization," *IEEE Trans. Med. Imag.*, vol. 36, no. 12, pp. 2546–2556, Dec. 2017.
- [40] Y. Yu, J. Jin, F. Liu, and S. Crozier, "Multidimensional compressed sensing mri using tensor decomposition-based sparsifying transform," *PLoS one*, vol. 9, no. 6, 2014, Art. no. e98441.
- [41] X. Yang, Y. Luo, S. Chen, X. Zhen, Q. Yu, and K. Liu, "Dynamic MRI reconstruction from highly undersampled (k, t)-space data using weighted Schatten p-norm regularizer of tensor," *Magn. Reson. Imag.*, vol. 37, pp. 260–272, 2017.

- [42] I. V. Oseledets, "Tensor-train decomposition," *SIAM J. Sci. Comput.*, vol. 33, no. 5, pp. 2295–2317, 2011.
- [43] R. Dian, S. Li, and L. Fang, "Learning a low tensor train rank representation for hyperspectral image super resolution," *IEEE Trans. Neural Netw. Learn. Syst.*, vol. 30, no. 9, pp. 2672–2683, Sep. 2019.
- [44] Q. Xie et al., "Multispectral images denoising by intrinsic tensor sparsity regularization," in *Proc. IEEE Conf. Comput. Vis. Pattern Recognit.*, 2016, pp. 1692–1700.
- [45] B. Aubert-Broche, A. C. Evans, and L. Collins, "A new improved version of the realistic digital brain phantom," *NeuroImage*, vol. 32, no. 1, pp. 138–145, 2006.
- [46] M. Maggioni, V. K. atkovnik, K. Egiazarian, and A. Foi, "Nonlocal transform-domain filter for volumetric data denoising and reconstruction," *IEEE Trans. Image Process.*, vol. 22, no. 1, pp. 119–133, Jan. 2013.
- [47] R. D. Nowak, "Wavelet-based rician noise removal for magnetic resonance imaging," *IEEE Trans. Image Process.*, vol. 8, no. 10, pp. 1408–1419, Oct. 1999.
- [48] J. V. Manjon, P. Coupe, A. Buades, D. L. Collins, and M. Robles, "New methods for MRI denoising based on sparseness and self-similarity," *Med. Image Anal.*, vol. 16, no. 1, pp. 18–27, 2012.
- [49] P. Coupe, J. V. Manjon, M. Robles, and D. L. Collins, "Adaptive multiresolution non-local means filter for three-dimensional magnetic resonance image denoising," *IET Image Process.*, vol. 6, no. 5, pp. 558–568, 2012.



**Lizhen Deng** (Member, IEEE) received the BS degree in electronic information science and technology from Huaibei Coal Industry Teachers College, Huaibei, China, in 2007, and the MS degree in communication and information systems from the Nanjing University of Aeronautics and Astronautics, Nanjing, China, in 2010 and the PhD degree in electrical engineering from the Huazhong University of Science and Technology, China, in 2014. In 2014, she joined the Nanjing University of Posts and Telecommunications, Nanjing, China. Her current research interests

include image processing, computer vision, pattern recognition, and spectral data processing.



**Yuxin Cao** received the BS degree from the Chengxian College of Southeast University, majoring in Electronic Information Engineering, Nanjing, China in 2021. Currently, she is working toward the MS degree in Signal and Information Processing, Nanjing University of Posts and Telecommunications, Nanjing. Her research interests include medical image analysis, pattern recognition, image processing, and computer vision.



**Zhongyang Wang** received the BE degree in electronic and information engineering from the Nanjing University of Posts and Telecommunications, Nanjing, China, in 2017. He is currently working toward the PhD degree in signal and information processing in Nanjing University of Posts and Telecommunications. His current research interest is computer vision.



**Xiaokang Wang** (Member, IEEE) received the PhD degree in computer Architecture from the Huazhong University of Science and Technology, China, 2017. Currently, he is a professor with School of Computer Science and Technology, Hainan University, China. His research interests include parallel and distributed computing, Big Data, tensor computing, industrial Internet-of-Things, and cyberphysical-social systems.



**Yu Wang** (Member, IEEE) received the BE degree in network engineering from the National University of Defense Technology, ChangSha, China and the PhD degree in computer science from the School of Computer and Communication Engineering, University of Science and Technology Beijing, Beijing, in 2020. Currently, he is senior engineer with Science and Technology on Integrated Information System Laboratory, Institute of Software Chinese Academy of Sciences. His research interests include pattern recognition and deep learning.